ACS APPLIED MATERIALS & INTERFACES

www.acsami.org Research Article

Computational Characterization of the Structure, Energy, Strengths, and Fracture Resistances of Symmetric Tilt Grain Boundaries in Ice

Hang Li,* Thanh C. Phan, Ling Zhang, Shuozhi Xu, Ashraf Bastawros, Hui Hu, and Liming Xiong*

Cite This: *ACS Appl. Mater. Interfaces* 2025, 17, 2541−2555 Read Online

ACCESS | Metrics & More | Article Recommendations

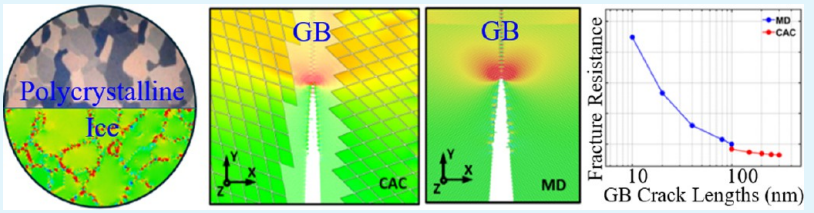

ABSTRACT: Using an interatomic potential that can capture the tetrahedral configuration of water molecules (H_2O) in ice without the need to explicitly track the motion of the O and H atoms, coarse-grained (CG) atomistic simulations are performed here to characterize the structures, energy, cohesive strengths, and fracture resistance of the grain boundaries (GBs) in polycrystalline ice resulting from water freezing. Taking the symmetric tilt grain boundaries (STGBs) with a tilting axis of ⟨0001⟩ as an example, several main findings from our simulations are (i) the GB energy, E_{GB}, exhibits a strong dependence on the GB misorientation angle, θ. The classical Read-Shockley model only predicts the $E_{GB} - \theta$ relation reasonably well when $\theta < 20°$ or $\theta > 45°$ but fails when $20° < \theta < 45°$; (ii) two "valleys" appear in the E_{GB}–θ landscape. One occurs at $\theta = 22°$ for $\Sigma14(\bar{2}3\bar{1}0)$ GB, and the other is at $\theta = 32°$ for $\Sigma26(\bar{3}4\bar{1}0)$ GB. These two GBs might be the most common in polycrystalline ice; (iii) all the STGB structures under consideration here are found to be a collection of edge dislocations with a Burgers vector of $\mathbf{b} = 1/3\langle 11\bar{2}0\rangle$. The core structure of this edge dislocation is composed of a pentagon and a heptagon atomic ring. The separation and orientation of the structure units (SUs) at the GB exhibit a strong dependence on θ; (iv) the length of an atomic bond within the SUs, rather than E_{GB} and θ which are often used in the literature, is identified as one controlling parameter that dictates the intrinsic GB cohesive strength; (v) characterization of the fracture resistance of the GB containing an initial crack is beyond the reach of nanoscale atomistic simulations but is feasible in concurrent atomistic-continuum (CAC) simulations that can simultaneously retain the atomic GB structure together with the long-range stress field within one model. The above findings provide researchers with a stepping stone to understand the complex microstructure of polycrystalline ice and its response to external forces from the bottom up. Such knowledge may be consolidated into constitutive rules and then transferred into the higher length scale models, such as cohesive zone finite element models (CZFEMs), for predicting how polycrystalline ice fractures at laboratory and even geophysical length scales.

KEYWORDS: *ice, grain boundaries, cohesive strength, fracture, atomistic and multiscale simulations*

1. INTRODUCTION

A mechanistic understanding of fracture in ice is not only important in engineering applications, such as deicing from airplanes, ships, wind turbines, and power transmission lines,[1−3] but also essential for predicting the behavior of atmospheric or glacier ice in geophysical science. The ice sheets resulting from water freezing in seawater, the atmosphere, or on the cold surfaces of engineering infrastructures are always polycrystalline in nature.[4] It has a very complex microstructure, being embedded with a large population of grain boundaries (GBs). Under external forces, these GBs act as preferred sites for crack initiation and growth. The failure of polycrystalline ice spans a wide range of length scales, including atomic-level bond ruptures, nanoscale void nucleation/coalescence on the GB, microscale GB crack growth, and then the shedding of the whole sheets at the macroscopic level. Clearly, the GB plays a central role in controlling the overall behavior of ice subject to external forces or deformation. A characterization of its GB energy (noted as E_{GB}), structure, cohesive strength, fracture resistance, and so on, thus becomes fundamentally necessary if one desires to understand how ice fractures from the bottom up.

From an experimental point of view, a direct measurement of the energy, structure, cohesive strengths, and fracture

Received: October 7, 2024
Revised: December 15, 2024
Accepted: December 18, 2024
Published: December 26, 2024

https://doi.org/10.1021/acsami.4c17074
ACS Appl. Mater. Interfaces 2025, 17, 2541−2555

resistance of the GB in ice is nontrivial, although this might have been well achieved in metals or alloys.[5] Taking the experimental calibration of E_{GB} as an example, to the best of our knowledge, although the first experimental study of ice GB energies was performed using plastic replicas of the ice surface[6] more than 40 years ago, the values obtained from such a low-resolution approach are still being used up to today. By considering only the low-angle GBs (LAGBs) and measuring their energy at a temperature near the melting point, one main finding from that pioneering research is that E_{GB} exhibits a dependence on the GB misorientation angle, θ. This, however, may not yet cover the full complexity associated with the E_{GB}–θ relation because the GB misorientation angles in ice span a significantly wider range instead of only LAGBs. Later on, as an extension of the above attempt, through an indirect experimental method, Suzuki and Kuroiwa[7] measured the E_{GB} in an ice sample containing a well-designed triple junction and characterized its dependence on the misorientation angle (noted as θ) ranging from 0 to 180°. This approach was built upon three key components: (i) considering the GB energy as an interfacial tension; (ii) the interfacial tensions, noted as γ_1, γ_2, and γ_3, of the three GBs at the triple junction, are then related with the GB misorientation angles, θ_1, θ_2, and θ_3 through an equilibrium equation; and (iii) if one GB (noted as the reference GB) in the sample is carefully chosen and has a well-known interface tension, with the three misorientation angles being directly measurable, the energies of the other two GBs in the triple junctions can be then calculated. The two main observations from such an indirect measurement are (a) the E_{GB}–θ relation follows the Read-Shockley equation when $0° < \theta < 15°$; and (b) the GB energies at $\theta = 90°$ and $\theta = 180°$ are significantly lower than E_{GB} at any other misorientation angles.

Thereafter, in a more systematic study, Nasello and co-workers[8] performed similar indirect experiments to examine whether a classical coincidence site lattice (CSL) theory could be used to explain the observed GB misorientation angle dependence of E_{GB} in ice. According to Herring's theory[9] of the surface energy balance at the GB groove, E_{GB} was determined thereby measuring the root angles of the grooves formed at the intersection between a GB and the free surface. In these experiments, the grooves were copied by plastic replicas, and then the topographic configuration of the GBs participating in the formation of this groove was revealed with a laser confocal 3D microscope. From such experiments,[6,7] the values of E_{GB} for a variety of GBs with their misorientation angles ranging from 10 to 90° in pure and also chemically doped polycrystalline ice samples annealed at −5 and −18 °C were obtained. It was found that the experimentally measured E_{GB}–θ relation[10] corresponds well to the CSL prediction. Despite that, it remains challenging to use such replica-based experiments to explore the full space of the misorientation angles because many GBs in ice are not even visible on the ice sample surfaces, which appear to be as clear as liquids. It becomes even more challenging if one desires to (i) isolate each individual GB from its complex microstructure environments; (ii) deform it under a controllable stress for measuring its cohesive strengths and fracture resistance; and (iii) probe the mechanisms underlying the GB fracture. To address this challenge, as a valuable supplement to experiments, the development of computational approaches that can model the ice GB structure and its response to external forces becomes necessary.

At the macroscopic level, one numerical method that enjoys the most popularity in modeling the fragmentation of materials is the cohesive zone finite element method (CZFEM).[11] It is based on the concept of a cohesive zone model (CZM),[12] which adds a zone of zero thickness ahead of the crack tip to describe the fracture process by avoiding the stress singularity in linear elastic fracture mechanics (LEFM). In CZFEM, the cohesive zone is idealized as two cohesive surfaces that are held together by cohesive traction. The material fracture is described as the separation of those two surfaces according to a cohesive law that relates the cohesive traction to the displacements of them with respect to each other. For polycrystalline ice[13,14] modeled by CZFEM, the 3D sample is treated as a deformable heterogeneous solid containing crystalline ice grains bonded with each other through cohesive zones.[14] Individual grains could not fracture and were assumed to be linearly elastic. Different from the traditional traction-separation formulation that does not distinguish between tangential and normal loads, a potential-based CZM, noted as the PPR-CZM developed by Park, Paulino, and Roesler[15] with 8 parameters (fracture energy, cohesive strength, brittleness, and so on) to define the interface behavior along normal and tangential directions was used to simulate the fracture of polycrystalline ice.[14] This model was demonstrated to have the capability of reproducing the results from uniaxial compression and tension tests by capturing damage accumulation, crack propagation, and even GB strengthening in granular ice. The results from such CZFEM-based simulations are promising but still need to be taken cautiously because: (i) the CZM parameters were chosen by matching experimental results for samples with one particular microstructure obtained from one specific freezing condition, which might not be transferable; (ii) it is a mathematical approximation of the underlying physical processes based on continuum mechanics without considering the fine-scale structure/energy states at the GBs; and (iii) the same set of model parameters is assigned to all the cohesive zones. This does not reflect the variability of the GB cohesion in real polycrystalline ice. Clearly, a further improvement of the predictive capability of such CZFEM requires a characterization of the ice GB energy, cohesive strength, and fracture resistance, as well as their dependence on the fine-scale structures at the GBs.

To meet this need, taking the GB in ice with a tilting axis of ⟨0001⟩ as an example, in this work, we perform full molecular dynamics (MD) and also concurrent atomistic-continuum (CAC) simulations to correlate ice GB misorientation angle, structure, as well as energy with its cohesive strength and fracture resistance. The remainder of this paper is organized as follows. The model setup is presented in Section 2. The simulation results are then delivered in Section 3. It contains three components: (a) a characterization of the misorientation angle, θ, dependence of the GB energy, E_{GB}, and its correspondence to the atomic-level GB structure; (b) quantification of the GB cohesive strength as well as its correlation with θ, E_{GB}, and the critical bond lengths at the GB; (c) a measurement of the GB fracture resistance and its dependence on the initial crack length ranging from nanometers up to submicrons. Thereafter, this paper ends with a summary of our major findings and future attempts in Section 4.

https://doi.org/10.1021/acsami.4c17074
ACS Appl. Mater. Interfaces 2025, 17, 2541−2555

2. METHODS AND MATERIALS

Up to date, over 15 different solid-state crystal structures in ice have been identified.[16,17] Hexagonal ice, noted as I_h ice, is the most common form of crystalline water on Earth.[4] Each water molecule in I_h ice is surrounded tetrahedrally by four nearest neighbors centered about 6 molecules forming an $O-O-O$ angle of approximately 109.5°. The atomic structure of monocrystalline I_h ice was first determined by X-ray diffraction.[18] A schematic sketch of the unit cell composed of 16 water molecules in monocrystalline I_h ice is shown in Figure 1. It is in a hexagonal column with its top and bottom being in

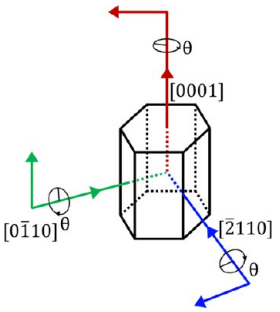

Figure 1. Schematic sketch of the crystallographic orientation in the unit cell of the I_h ice. For the GB under consideration in this work, the ⟨0001⟩ is selected as the rotational axis for building the model for a bicrystalline ice sample.

the basal planes with a normal direction of [0001], and six equivalent side faces being in the prism planes (see Figure 1). Instead of explicitly modeling each hydrogen and oxygen atom in a water molecule, a monatomic model for water molecules is employed here. The tetrahedral, short-ranged interactions among the monatomic water molecules are characterized by employing a well-established mW force field.[19−21] In detail, mW mimics hydrogen- and electrostatic-bonded structures in water using a three-body nonbond angular-dependent term that encourages tetrahedral molecular configuration in crystalline ice. It has only short-range interactions yet reproduces the energetics, structure of liquid water, ice nucleation, and growth with comparable accuracy to a fully atomistic model but at less than 1% of the computational cost of it.[19,20] mW has been successfully used to investigate the nucleation of ice from bulk water[19] and solutions[21] with two orders of magnitude higher computational efficiency than fully atomistic simulations. As far as the mechanical properties of ice are concerned, it was shown[22] that the mW force field predicts experimentally comparable stiffness, Young's modulus, and shear moduli. Although it underestimates the anisotropy of ice,[22] we believe an inaccurate description of the anisotropy in ice by mW will not alter the main conclusion from this work because bicrystals are modeled here. In such samples, the anisotropy associated with each grain will be averaged out anyway, even if one uses a higher-fidelity force field to better describe the anisotropy in ice. Thus, we argue that the deployment of the mW force field will enable a characterization of the ice GB structure/properties to be not only reasonably accurate but also computationally efficient.

The bicrystalline simulation cell containing an individual GB is then constructed as shown in Figure 2. In detail, the bicrystal model is built by combining two crystalline grains with different crystallographic orientations (Figure 2). The GB plane is aligned with the $y-z$ plane. Figure 2 shows the schematic sketch for a simulation cell containing one $(\bar{1}2\bar{1}8)\langle 0\bar{1}10\rangle$ GB. The misorientation angle θ is the angle between the ⟨0001⟩ directions of those two grains. The whole simulation cell has dimensions of 100, 50, and 8 nm along the x, y, and z directions, respectively. It contains about one million atoms in total. The simulations were conducted using the large-scale atomic-molecular massively parallel simulator (LAMMPS).[23]

Periodic boundary conditions (PBCs) along the x, y, and z directions are applied when this model is used to calculate the GB energy, but the PBC along the x direction will be removed when a

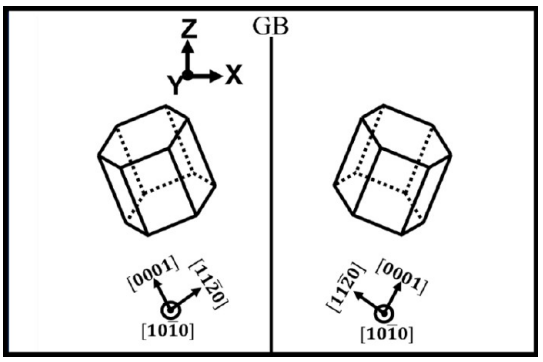

Figure 2. Sketch of the simulation cell for a bicrystalline model. The two grains in this model are rotated with respect to each other by an angle of θ. The rotation axis is the y axis and the GB plane is in the $y-z$ plane.

tensile loading is then applied on the two ends to calculate the GB cohesive strength and fracture resistance. In such tensile tests, only the PBCs along the y and z directions remain. It should be noted that although an application of the PBC along the x, y, and z directions implies periodically distributed grains and GBs, such a setup still predicts the GB structure and energy reasonably well because: (i) only the ground-state equilibrium GBs (EGBs) are considered in this work; (ii) both the internal stresses and the atomic configuration energy associated with such EGBs are localized by spanning a very short-range (see Figure 3); and thus, (iii) the presence of the periodic images will not affect the structure and energy of the EGBs. Nevertheless, as far as the GB cohesive fracture is concerned, the internal stresses ahead of the crack tip may span a significantly longer range than GB stress does. In such scenarios, the stress induced by the periodic images, especially those along the x directions, cannot be simply ignored, so the PBC along the x direction is removed when the simulation cell is used to measure GB cohesive strengths and fracture resistance.

3. SIMULATION RESULTS

3.1. Grain Boundary Energy. In order to characterize the ground-state GB energy and structures, an approach reported previously[24,25] is deployed. This approach includes rigid body translations and atoms deleting on the GB. The preceding operations generate hundreds of various initial STGB configurations. To determine the minimum configuration energy of the GBs with a wide range of misorientation angles, atomic annealing, and subsequent molecular statics computations using a nonlinear conjugate gradient algorithm for each GB with a particular θ have been performed. For each specific microscopic configuration, the GB energy (i.e., excess free energy) is calculated by

$$E_{GB} = \frac{1}{2A}(E_{total} - nE_{pristine}) \quad (1)$$

where n denotes the number of total number of the atoms (each atom represents a water molecule in mW) in the system, A is the area of the GB plane, E_{total} is the potential energy of the system for the given configuration with GBs, and $E_{pristine}$ is the energy per molecule in pristine hexagonal ice.

We have selectively incorporated solely the GB structures with the lowest energy while disregarding the higher energy structures, as they are considered metastable and have been omitted from the analysis. Here, we focus on the study of GB structure/properties at a temperature of 10 K because: (i) the repeating atomic structural units on the GBs in ice are found to be only clearly recognizable at 10 K and even lower

https://doi.org/10.1021/acsami.4c17074
ACS Appl. Mater. Interfaces 2025, 17, 2541−2555

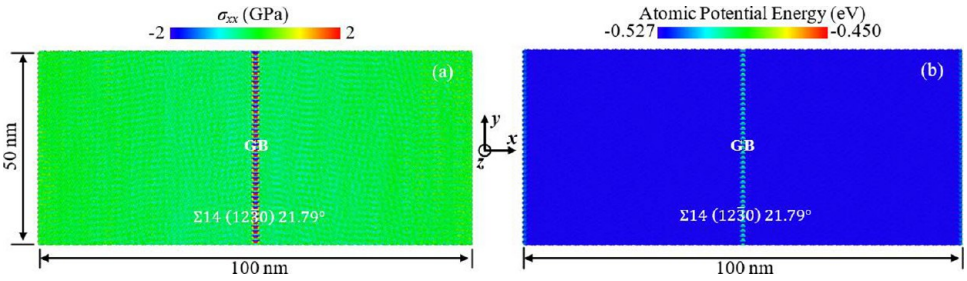

Figure 3. mW-based MD simulation results showing the short-range nature of (a) the internal stresses and (b) the atomic configuration energy of one sample of EGB in ice.

temperatures[26]; (ii) a reproduction of such repeating atomic structures on the GBs is important if one desires to quantitatively correlate the GB structural feature, atomic bond length, with its intrinsic cohesive strengths and fracture resistance; and (iii) such a quantitative correlation is important and will lay the characterization of the environmental temperature dependence of the ice mechanical properties on a firm basis.

For the particular STGB under consideration here, the energy, i.e., E_{GB}, resulting from our atomistic simulations using the mW force field and its dependence on the misorientation angle θ are plotted in Figure 4. Two representative GBs (Σ = 14 and 26), where the two valleys appear, are also marked in Figure 4. Quantitatively, the E_{GB} values at each particular θ are also summarized in Table 1.

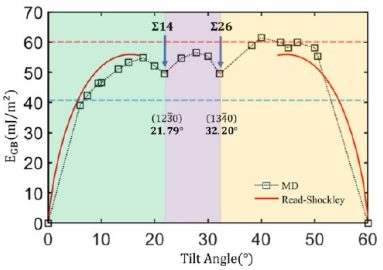

Figure 4. Atomistic simulation-predicted ⟨0001⟩ GB energy and its dependence on the misorientation angle θ in ice. The red line shows a fitting of the simulation results to the classical Read-Shockley models. For comparison purpose, data from experimental measurements of E_{GB} using the grooving technique are included as shown in blue and red dash lines.

Three main observations from Figure 4 and Table 1 are (1) E_{GB} exhibits a strong dependence on θ, it varies between 38 and 60 mJ/m^2 when the misorientation angles change from 0 to 60°; (2) as discussed before, due to the difficulty of exploring the full range of θ using the grooving techniques, the experimental measurements of E_{GB} can only provide us with a lower[27] (see blue dash line in Figure 4) and an upper[28] bound (see red dash line in Figure 4) of E_{GB}. An experimental characterization of the full complexity of the θ dependence of E_{GB} remains nontrivial. It can only be supplemented by high-fidelity simulations if a full-spectrum analysis of the θ dependence of E_{GB} becomes desired; (3) according to the E_{GB}–θ landscape in Figure 4, two clearly prominent valleys or cusps appear at Σ14(12$\bar{3}$0) θ = 21.79° and Σ26(13$\bar{4}$0) θ = 32.2°, respectively. It implies that among many ⟨0001⟩ STGBs in ice, those GBs with CSL values of Σ14 or Σ26 might be most common due to their considerably lower energy states.

Table 1. Simulation-Predicted [0001] STGB Energy and Its Dependence on CSL and θ

CSL and GB plane	θ (°)	E_{GB} (mJ/m^2)
Σ 182 (4 5 $\bar{9}$ 0)	6.01	38.98
Σ122 (5 6 1$\bar{1}$ 0)	7.36	42.21
Σ74 (3 4 $\bar{7}$ 0)	9.43	46.39
Σ38 (2 3 $\bar{5}$ 0)	13.17	51.09
Σ43 (5 8 1$\bar{3}$ 0)	15.18	53.19
Σ31 (4 7 1$\bar{1}$ 0)	17.90	54.78
Σ14 (1 2 $\bar{3}$ 0)	21.79	49.56
Σ13 (2 5 $\bar{7}$ 0)	27.80	56.57
Σ26 (1 3 $\bar{4}$ 0)	32.20	49.47
Σ7 (1 4 $\bar{5}$ 0)	38.21	58.91
Σ49 (2 11 1$\bar{3}$ 0)	43.57	59.93
Σ19 (1 7 $\bar{8}$ 0)	46.83	59.91
Σ37 (1 10 1$\bar{1}$0)	50.57	55.30

Moreover, in Figure 4, we also fit the simulation data into the classical Read–Shockley[29] model, which formulates E_{GB} as a function of θ in the framework of the theory of elasticity. The formula for the Read-Shockley model is shown in Eq. 2 as shown below. It was developed for LAGB with θ between 0 and 15° by considering it as a collection of dislocations.

$$E_{GB} = E_0\theta\left\{1 + \ln\left(\frac{b}{2\pi r_0}\right) - \ln(\theta)\right\},\quad r_0 = \frac{Gb}{4\pi(1-\mu)} \tag{2}$$

where $G = 3.4 \times 10^9$ Nm^{2-} is the shear modulus, $\mu = 0.41$ is the Poisson's ratio, and r_0 is the dislocation core radius and is between b and $5b$,[30] with b being the norm of the Burgers vector of the dislocation in ice.

A fitting of our simulation data into the above model in Figure 4 shows that the E_{GB}–θ relation can be divided into three regimes (noted as Regimes-I, II, and III colored green, purple, and yellow, respectively). For the regime of 0° < θ < 15° (Regime-I) or 45° < θ < 60° (Regime-III), the simulation-predicted E_{GB}–θ relation fits into the Read–Shockley model very well. A fitting of the simulation data into Eq. 2 provides us with an opportunity of (a) calibrating the models for the E_{GB}–θ relation at the continuum level, which leads to b = 4.52 Å, $r_0 = 0.6b$ for LAGBs but b = 7.36 Å and $r_0 = 0.56b$ for HAGBs; and (b) expanding the Read-Shockley models by including higher order terms into the formulation for the E_{GB}–θ relation to describe the misorientation angle dependence of E_{GB} not only for LAGBs or HAGBs but also for GBs with intermediate misorientation angles, such as 15° < θ < 45° (Regime-II) in Figure 4. This has been previously achieved[31]

https://doi.org/10.1021/acsami.4c17074
ACS Appl. Mater. Interfaces 2025, 17, 2541–2555

for the GBs in metals and will be expanded for ice GBs in our future attempts.

3.2. Grain Boundary Structures. To characterize the GB structure in ice at a high resolution, the atomic structures resulting from the simulations are visualized using OVITO.[32] The extended common neighbor analysis (CNA)[33] is performed to probe the GB structure and its evolution. The structures of the GB under consideration here can be considered as a collection of structure units (SUs), which are also noted as the kite structures commonly observed in tilt GBs.[34] Such SUs do not carry any dangling bonds and have been also identified at ⟨0001⟩ STGBs in several other materials, such as GaN and SiC.[35,36] Similar concepts will be adapted here for ice GB structure analysis.

Figure 5 presents the equilibrium atomic structures of the ⟨0001⟩ STGBs with their misorientation angles ranging from

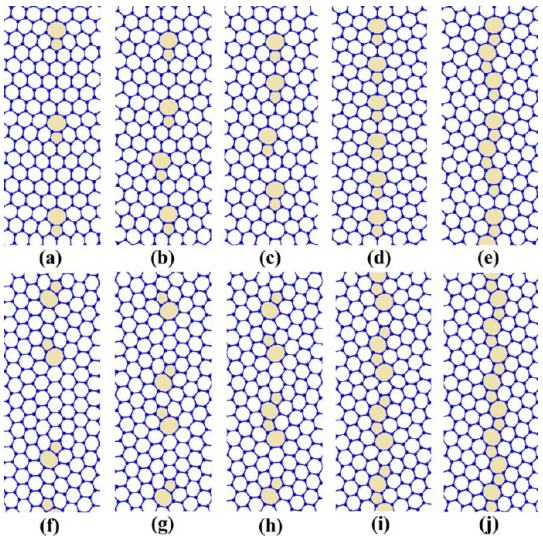

Figure 5. Atomic structures of ⟨0001⟩ tilt GBs with different misorientation angles. The pentagons and heptagons are highlighted in yellow. The bonds between water molecules are displayed to illustrate the GB structures: (a–e) θ = 9.43, 15.18, 17.9, 21.79, and 27.8°, respectively; (f–j): θ = 50.57, 46.83, 43.57, 38.21, and 32.2°, respectively.

9.43 to 50.57°. Several main findings from Figure 5 are (a) the pairs of pentagon (5-atom ring) and heptagon (7-atom ring), noted as "57" and "57/57" (see details in Figure 5), or the pairs of inclined pentagon and heptagon (noted as "57 + 5c–") form the base structures of the STGBs under consideration here; (b) when θ = 9.43, 15.18, 17.9, 21.79°, the GB contains only the "57" units. The separation between these "57" SUs decreases upon the increase of θ (Figure 5a–d); and (c) when θ = 32.2° and above, the GBs are composed of "57 + 57–". These "57 + 57–" are connected with each other, but the separation between them will increase upon the further increase of θ for θ > 32.2°. The atomic configurations in "57" and "57 + 57–" SUs correspond to the core structures of $a/3\langle 11\bar{2}0\rangle$ (see the inset pictures in Figure 5) and $a/\sqrt{3}\langle 11\bar{2}0\rangle$ edge dislocations, respectively, where a is the lattice constant. In this way, all the STGBs shown in Figure 5 can be considered as a collection of dislocations.[29] The dislocation densities in LAGBs (θ < 22°) or HAGBs (θ > 45°) are significantly higher than that in the GBs with intermediate misorientation angles (22° < θ < 45°). This observation also explains why the classical Read-Shockley model fits well into the simulation data only for LAGBs or HAGBs (Figure 4) because it was developed from the theory of elasticity, which considers only the dislocation interaction with each other through long-range stresses. For the intermediated STGBs, the core of the dislocations in them get close to each other. Each dislocation core carries a high local stress and induces a strong short-range interaction. This needs to be taken into account if an expansion of the Read-Shockley model becomes desired for fitting it into the atomistic-simulation-predicted E_{GB}–θ relation across a wide range of θ.

To correlate the GB structure with (θ) and its CSL value (noted as Σ), Figure 6 lists the smallest repeating SUs (see column-3 of Figure 6) identified from our atomistic simulations for the STGBs with a wide range of θ (see column-1 of Figure 6) and Σ (see column-2 of Figure 6). An identification of the smallest repeating SUs provides us with opportunities of (i) interpreting the previous X-ray diffraction (XRD) topographic observations of the large-angle GB in ice,[37,38] where the facets on the HAGBs seen in XRD might be mapped as a collection of the atomic SUs summarized above; (ii) constructing the atomistic models for a variety of complex GBs by simply using these smallest SUs as building blocks. For instance, to construct a curved GB with one segment of it carrying a misorientation angle of 7.36° and the other segment of 9.43°, one can simply repeat the "57666" (each SU is composed of one "57" unit together with three "6" and then periodically repeatable) unit for the first segment and then "5766" (each SU is composed one "57" unit together with two "6" and then periodically repeatable) for the second, followed by an assembly of these two segments and then a relaxation; (iii) fingerprinting the GB structures in realistic polycrystalline ice samples by using these SUs as descriptors; (iv) consolidating them into representative volume elements (RVEs), which in turn, can be used for characterizing the GB properties, such as cohesive strengths, fracture resistance, vibrational properties, and so on. For example, according to our analysis to be discussed below, the cohesive strengths of STGBs can be well correlated with the shortest bond length (see column 5 in Figure 6) in a "57" SU, rather than E_{GB} or θ in common wisdom.

3.3. GB Cohesive Strengths. After obtaining the minimum-energy configuration, the atomistic model is then annealed using MD in the canonical (NVT) ensemble for 50 ps at a temperature of 10 K with a time step of 5 fs. With the atomic structure being fully relaxed, a rate of 10^{-5} ps^{-1} uniaxial tension is then applied on the two ends of the sample to deform it. The tensile loading is along a direction (x direction in Figure 2) normal to the GB plane for quantifying the GB cohesive strength. The deformation is realized through a constant uniaxial strain rate loading in an NVT ensemble. That is, the two ends of bicrystals along the x direction are fixed and then moved along the positive and negative x direction perpendicular to the GB plane (Figure 2). To determine the GB cohesive strength, as a post-process, the system stress is calculated using the Virial formulas.[39] During such a uniaxial tensile test, the strain is defined as $\varepsilon = \delta l/l$; the change (δl) in the sample dimension is divided by its initial length (l) along the loading direction, i.e., the x direction in Figure 2.

Here, we define the GB cohesive strength as a critical stress at which a crack starts nucleating at the GB. It corresponds to a stress required for initiating a Mode-I crack on the GB. The simulation-predicted stress–strain (σ–ε) curves of the ⟨0001⟩

https://doi.org/10.1021/acsami.4c17074
ACS Appl. Mater. Interfaces 2025, 17, 2541–2555

θ	Σ	Structural units	Structure	Bond length(Å)
0°	1		6	2.702
6.01°	182		576666	2.829
7.36°	122		57666	2.823
9.43°	74		5766	2.829
13.17°	38		576	2.813
15.18°	43		576576(57)6	2.824
17.9°	31		57576(57)6	2.826
21.79°	14		57	2.770
27.80°	13		57/5757	2.792
32.20°	26		57/57	2.705
38.21°	7		$57^{+}57^{-}6$	2.799
43.57°	49		$57^{+}657^{-}66$	2.915
46.83°	19		$57^{+}657^{-}666$	2.835
50.57°	37		$57^{+}6657^{-}66666$	2.870
60	2		6	2.702

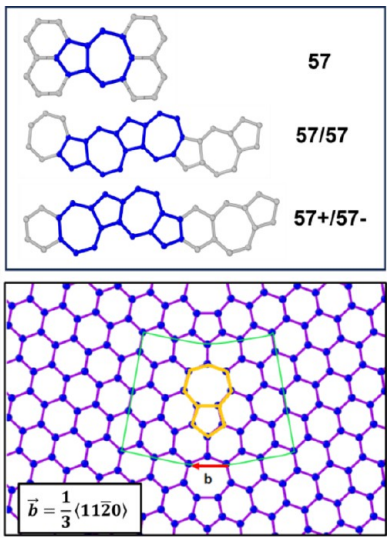

Figure 6. Smallest repeatable structural units for ⟨0001⟩ GBs, where the units of "57" are colored in pink, the units of "6" are colored in blue, and the units of "6−" are colored in yellow, respectively. Inset pictures show the atomistic structure of "57", "57/57", "57+/57−", "6", "6−", and the Burgers circuit around a "57" unit, respectively.

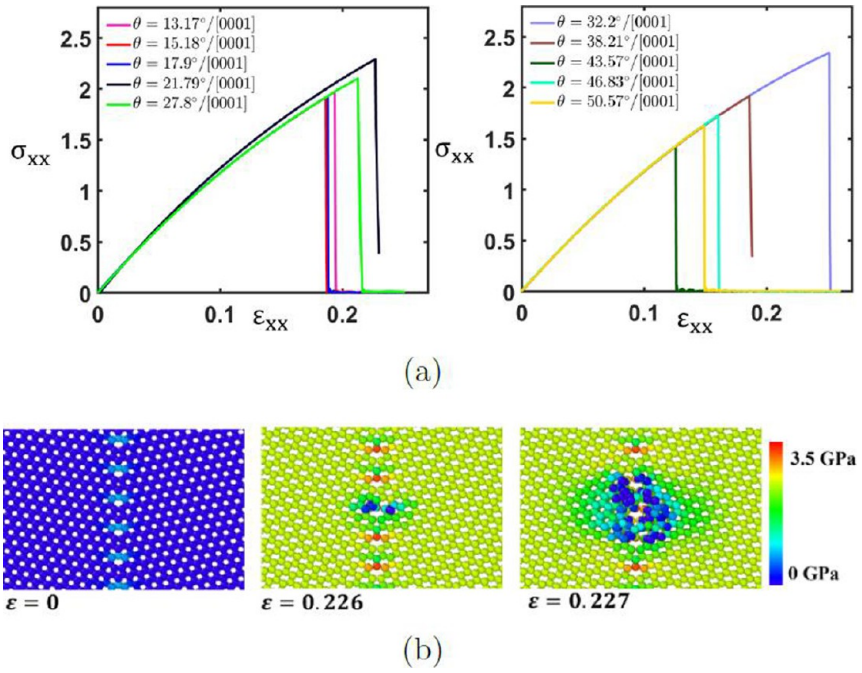

Figure 7. Simulation-predicted tensile deformation behavior of ⟨0001⟩ GBs with (a) $\theta < 30°$ and $\theta > 30°$; (b) strain sequences of the atomic structure and stress evolution around the GB with a misorientation anlge of 21.79° under tension. The vertical axis in (a) is in a unit of GPa.

GB under tension are shown in Figure 7. The tensile deformation behavior of five ⟨0001⟩ GBs with $\theta < 30°$ is shown in Figure 7a and that of another five GBs with $\theta > 30°$ is shown in Figure 7b, respectively. When the tensile strain is (∼5%) or below, all the GBs behave in a linear elastic manner as expected. At this stage, the variation in Young's modulus for different GBs is negligible. Given that Young's modulus for single crystalline ice along [0001] directions is around 11 GPa at 0 K, the simulation-predicted elastic deformation behavior is consistent with that from experiments[40] and high-fidelity MD simulations using TIP4P potential[41] which explicitly models the interactions between oxygen and hydrogen atoms in water molecules. The Young's modulus predicted here is also in the same order as that from MD simulations using many other different empirical potentials,[22] where the Young's moduli for single-crystalline ice were found to be in a wide range spanning from 12 to 14 GPa. Thereafter the elastic deformation state, with the continuous increase of tension, the stresses arrive at a peak value, and then a sudden drop of it is observed for all the GBs. This sudden drop corresponds to the failure of the GBs through a brittle fracture manner, whereby the GB rupture occurs abruptly without any noticeable prior alteration in the elongation rate.

As evidence that the peak stress does correspond to the crack initiation at the GB, Figure 7b presents the snapshots of the strain sequences of the atomic arrangements (atoms are color-coded with the stress component along the tensile direction) for a representative GB, i.e., the Σ14 $(12\bar{3}0)$ GB

https://doi.org/10.1021/acsami.4c17074
ACS Appl. Mater. Interfaces 2025, 17, 2541−2555

with a misorientation angle of 21.79°. It is seen that (i) before the tensile strain is applied, at $\varepsilon = 0$, all the atoms away from the GB are in dark blue (zero stress). This means a good equilibration of the bicrystalline atomistic model before it is deformed. Also, those atoms that belong to the "57" SUs are in light blue, which means the presence of an initial residual stress at the GBs due to the lattice mismatch nearby; (ii) when the applied tensile strain is increased up to $\varepsilon = 0.226$, the peak stress appears at the stress−strain curve for the GB with 21.79° (see the black curve in Figure 7a). Correspondingly, an "embryo" crack starts to nucleate at the GB. The atoms ahead of the two tips of this crack are in red, which suggests an atomic stress at a level of 3.5 GPa on the GBs. On the two surfaces of this crack, the atoms are in blue (zero stress), which means a significant reduction of the atomic interaction there and then the initiation of a crack; and (iii) upon a slight increase of the applied tensile strain to $\varepsilon = 0.227$, the newly nucleated crack at the GB starts to grow along the GB. As a consequence, more atoms participate in the formation of the crack surface and are now in blue. Similar atomic arrangement and local stress evolution have been observed in all the other GBs subject to a tensile loading along the direction normal the GB plane. This confirms that the peak stresses identified in Figure 7 can be recognized as the GB cohesive strengths for detecting crack initiation in perfectly structured GBs containing no pre-existing defects.

Another observation in Figure 7a, b is the GB with misorientation angles of 21.79 and 32.2° exhibit notably higher cohesive strengths than all the other GBs. Given that these two GBs have the lowest GB energy (see the E_{GB}−θ landscape in Figure 4), this observation seems to imply that there might exist a one-to-one correspondence between the GB cohesive strength and its energy. To test this hypothesis, Figure 8 shows the plots about the correlation between the cohesive strengths and the energy resulting from our atomistic simulations for two types of GBs (⟨0001⟩ GB in Figure 8a and ⟨10$\bar{1}$0⟩ GB in Figure 8b). Surprisingly, the simulation data in Figure 8a (⟨0001⟩ GB) indeed suggest an inversely linear correlation between the GB cohesive strength and E_{GB}, i.e., the lower E_{GB}, the higher cohesive strength, but the simulation data in Figure 8b (⟨10$\bar{1}$0⟩ GB) significantly scatter and do not follow any trend. Therefore, we cannot simply use the E_{GB} as an indicator of the cohesive strengths of all of the GBs. To understand why the cohesive strengths of the ⟨10$\bar{1}$0⟩ GB do not correspond well to its energy, Figure 8c shows the atomic structures of this GB with a few different misorientation angles. Clearly, compared with the structures of ⟨0001⟩ GB (Figures 5 and 6), the structure of ⟨10$\bar{1}$0⟩ GB is much more complicated. It does not contain a well-recognizable "57" or "57+/57−" units. As a consequence, for ⟨0001⟩ GB, there exists a well-defined one-to-one correspondence between E_{GB} and its structure. By contrast, for ⟨10$\bar{1}$0⟩ GB, several GBs with different misorientation angles can have similar E_{GB}. Based on the above observations, we conclude: (a) E_{GB} can be only used as an indicator of the GB cohesive strength when the structures of the GBs under consideration can be well-defined and differentiated from each other; (b) there is no one-to-one correspondence between E_{GB} and GB cohesive strengths if the GB structure is complex. This finding is consistent with the conclusion from the study[42] where the properties of the nonequilibrium GBs in alloys are not always necessarily related to E_{GB}.

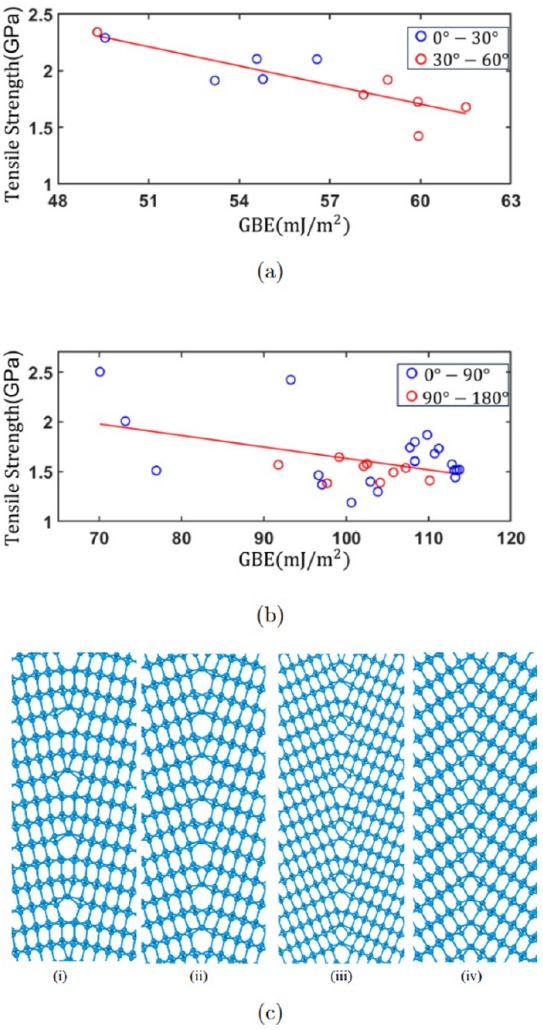

Figure 8. (a, b) a correlation of the GB cohesive strengths with GBE for ⟨0001⟩ and ⟨10$\bar{1}$0⟩ GBs, respectively; (c) atomic structure of ⟨0$\bar{1}$10⟩ GB with a misorientation angle of (i) 23.07°, (ii) 34.05°, (iii) 44.42°, and (iv) 62.96°, respectively.

We believe that the GB structure, rather than E_{GB}, dictates its properties (cohesive strengths, fracture resistance, and so on). To identify the structure parameter that controls the GB cohesive strengths, we measure and monitor the changes in the bond lengths on the GBs during their deformation. Results show that, for both ⟨0001⟩ and ⟨10$\bar{1}$0⟩ GBs, cracks always nucleate due to the breaking of one particular atomic bond (indicated by the arrow in the inset pictures of Figure 9a,b). It is an atomic bond in a "57" SU, is located within the 7-atom ring, and has the farthest distance away from the center of the 5-atom ring. Figure 9 shows that the cohesive strengths can be well correlated with the initial lengths of this bond in both ⟨0001⟩ and ⟨10$\bar{1}$0⟩ GBs. In detail, the cohesive strengths of the ⟨0001⟩ and ⟨10$\bar{1}$0⟩ GBs are linearly proportional to the initial strengths of this critical bond. A linear fitting of the simulation data is also provided in Figure 9a,b for eye guidance. Clearly, the GB cohesive strength decreases upon the increase in the initial length of this critical bond. The cohesive strength of a ⟨0001⟩ is in a perfectly linear inverse relationship with respect to the length of this critical bond. Quantitatively, in Figure 9a, for the LAGBs with the critical bond lengths of 2.83, 2.79, and 2.77 Å, the cohesive strengths are found to be 1.87, 2.1, and 2.29 GPa, respectively. For the ⟨10$\bar{1}$0⟩ GB, although the data is

https://doi.org/10.1021/acsami.4c17074
ACS Appl. Mater. Interfaces 2025, 17, 2541−2555

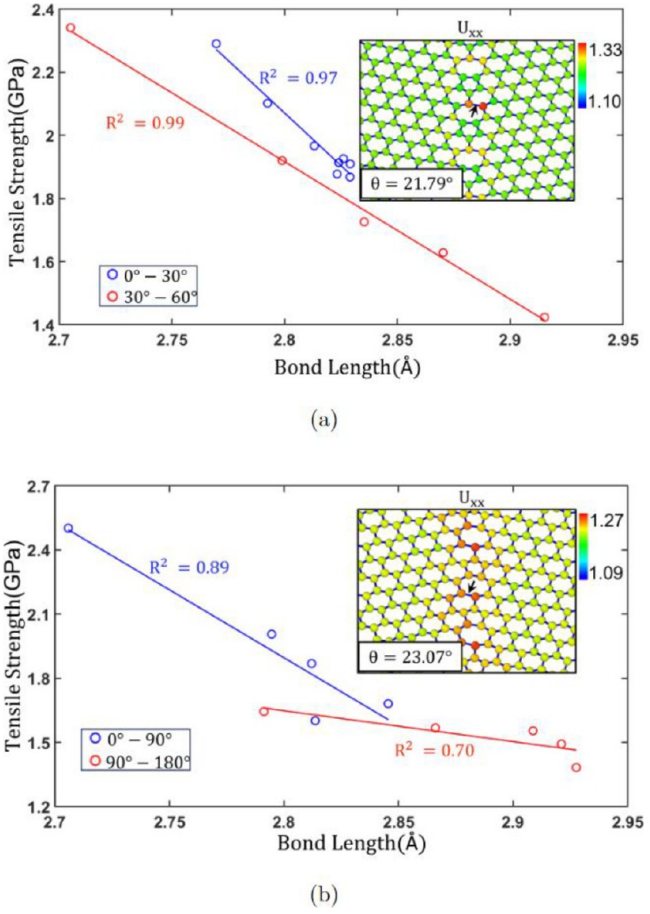

Figure 9. Correlation between the GB cohesive strength and the critical bond lengths for (a) ⟨0001⟩ and (b) ⟨10$\bar{1}$0⟩ GBs. The atoms in the inset pictures are color-coded with the magnitude of their displacement along the tensile direction. The black arrow indicates the critical bond within "57" SU.

slightly scattered, it still obeys the linear correlation reasonably well. One reason that this critical bond length can be used as an indicator of the cohesive strengths of both GBs is that it indicates the level of local strain at the GB. An increase in it means an elevated structure distortion initially and, in turn, a reduction of the GB cohesive strength. Thus, we believe the GB cohesive strength is closely related to the local strain within the GB. This is missing in many continuum models for polycrystals where the ground-state GB energies are always assumed. It needs to be incorporated into higher-length scale models, such as CZFEM if one desires to predict the GB crack nucleation without smearing out the underlying mechanisms.

3.4. GB Fracture Resistance. Here, we choose the critical stress intensity factor, noted as K_{IC}, to characterize the GB fracture resistance because: (a) according to the classical theory of fracture mechanics,[43] K_{IC} is a fundamental parameter used to characterize a material's resistance to fracture. It is a measure of a material's ability to resist crack propagation under mode-I loading conditions. Physically, K_{IC} represents the maximum stress intensity factor that material can withstand before a crack propagates catastrophically; (b) it is an intrinsic material property, influenced by microstructures, temperature, strain rate, and so on; (c) the displacement-controlled tensile loading imposed on our simulation cell is controlled by K_I. This enables us to determine K_{IC} as a critical value of K_I, above which the imposed displacement field will cause catastrophic failure of the GB. As shown in Figure 10, a line crack with an

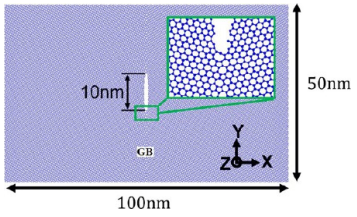

Figure 10. Atomistic model setup for measuring the fracture resistance of a GB containing an initial crack: the atomic interactions across the initial crack surfaces are turned off and a uniform tensile strain is imposed on the sample along x direction.

initial length of 10 nm is introduced on the ⟨0001⟩ GB by turning off the atomic interaction across the initial crack surface. The simulation cell is then stressed along the direction perpendicular to the GB until it fails.

Figure 11a shows the stress–strain curves resulting from such tensile deformation simulations for the ⟨0001⟩ GB with a variety of misorientation angles, θ, but containing the same 10 nm-long initial crack. The peak stresses in these curves correspond to the onset of crack growth. A correlation of the peak stress with the critical atomic bond length is also attempted here, as shown in Figure 11b. Different from what has been observed in Figure 9, the data in Figure 11b exhibit a large scatter. It implies that even if we use the critical bond length as the indicator, i.e., the GB fracture resistance cannot be well characterized using the computational setup shown in Figure 10. This could be attributed to several reasons: (a) the initially introduced crack carries a long-range stress field (Figure 11c). It does not decay to zero until hundreds of nanometers or even microns. The long-range stress field associated with the crack in the simulation cell overlaps with the stress field induced by its periodic images in the neighboring simulation cells due to the deployment of PBCs. This in turn causes uncontrollable complications in the critical stress calculations when the crack starts to grow; (b) the tensile loading is applied on the sample through imposing a uniform tensile strain on the sample along the x direction. This differs from the displacement field around a Mode-I crack in linear elastic fracture mechanics (LEFM).[43] Therefore, it is not surprising that the resulting fracture resistance does not converge. An elimination of the above two artifacts necessitates a computer model that can: (i) retain the atomistic structure on the GBs; (ii) accommodate the long-range stress field ahead of the GB crack tip in a submicrometer- or micrometer-sized sample; and (iii) facilitate us to impose a displacement field derived from LEFM on the sample boundaries due to its capability of scaling up in lengths.

Our concurrent atomistic-continuum (CAC) method which has been developed since 2009[44−49] can be one such approach to satisfy the above three needs. Distinct from many concurrent methods that directly combine MD and classical FE, fundamental to CAC is a formulation that unifies atomistic and continuum descriptions of materials through generalizing Kirkwood's statistical theory of transport processes.[50−53] The atomic displacement field in it is expressed as the sum of a continuum-level lattice cell deformation and a discrete sublattice deformation. In this way, the continuum quantities (mass, energy, and stress) can be defined in terms of atomic

https://doi.org/10.1021/acsami.4c17074
ACS Appl. Mater. Interfaces 2025, 17, 2541−2555

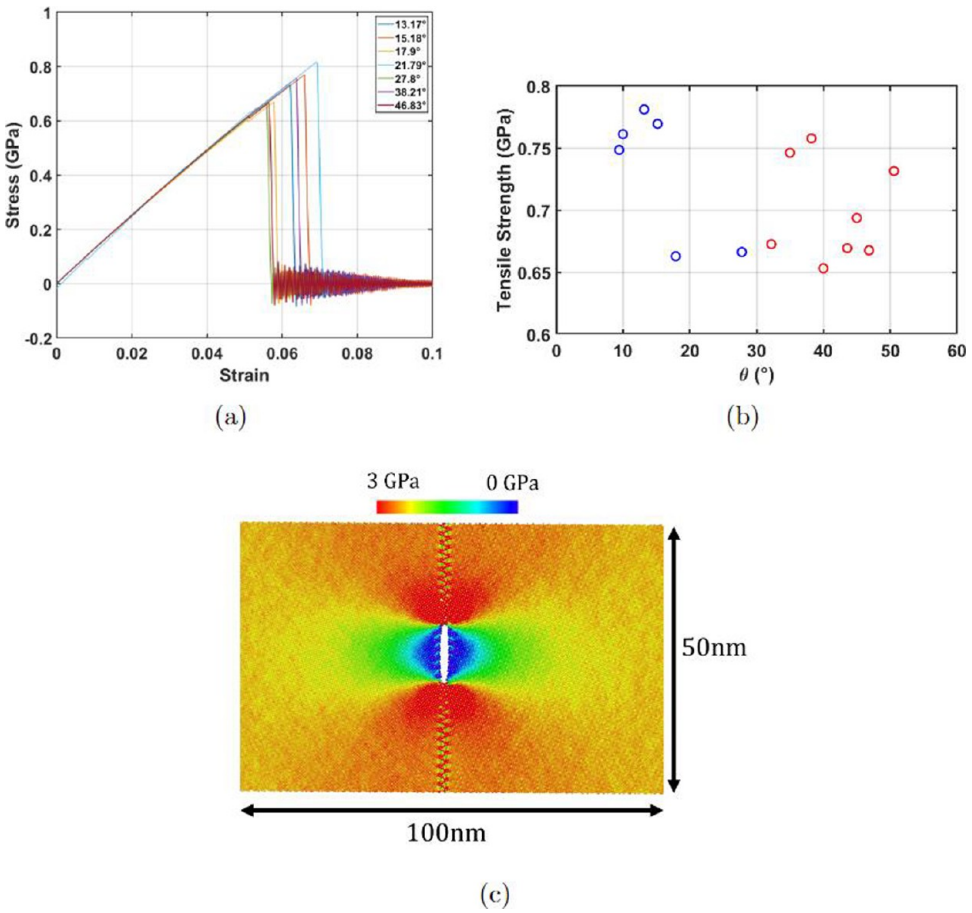

Figure 11. Characterizing the fracture resistance of the GBs containing a crack under tension: (a) stress−strain curves for a variety of GBs at different θ under tension; (b) correlation between the ultimate tensile strength and the critical atomic bond lengths within the GBs with different θ; and (c) the long-range internal stress (the σ_{xx} component along the tensile direction) carried by an initial crack, indicating that a limited simulation cell size in a fully atomic model may pollute the simulation results.

forces, displacements, and velocities. The atomistic-informed balance equations were then derived.[54−56] They are identical in form to those in continuum theories. Thus, continuum modeling techniques, such as FE, can be used to solve them. The discretization of a sample into FEs leads to a coarse-grained (CG) description of the materials. Two key features of this CG model are (1) it requires interatomic potential as the only constitutive rule and (2) the FE in it conforms to the geometry of a material's primitive cell. This element ensures that following nucleation dislocations and cracks can migrate along the FE boundaries aligned with the slip and cleavage planes, respectively. The combination of CG and atomistic leads to a CAC model, which can pass dislocations and cracks between atomistic and continuum in a self-consistent manner.[46,48] As such, at a fraction of the cost of full MD, without the need for additional numerical treatments, it can be a unique platform for characterizing the fracture resistance of the atomically structured GBs, which contain cracks with lengths ranging from several nanometers to micrometers and above. Several representative significant developments of the CAC method by other groups after 2009 include but are not limited to (i) expanding it for modeling polyatomic crystals in which each primitive cell contains more than one atom[57]; (ii) implementing a quasi-static algorithm into it for carrying out energy minimization[58]; and (iii) furnishing it with schemes for passing short wavelength waves from the atomic to continuum domains.[59,60]

As a preliminary attempt, here, we perform CAC simulations of crack growth along the ⟨0001⟩ GB with a misorientation angle of θ = 21.79°. Figure 12a presents the CAC setup for simulating the crack growth at a GB in a bicrystalline sample under Mode-I loading. The atomistic structure of the GB is retained, and an FE driven by the same mW interatomic potential is deployed in the region away from the GB to eliminate the majority of the atomistic degrees of freedom (see Figure 11a for the CAC computer model setup). This provides us with an opportunity to study the cracks with their lengths ranging from several nanometers up to hundreds of nanometers and even microns at a fraction of the cost of full MD simulations. The unique FE employed in CAC has not only naturally considered the crystal anisotropy in I_h ice but also allows dislocation emission/migration or crack growth into the far field if there would be any. In this way, GB crack growth as well as the slip band formation mediated by the long-range dislocation migrations underneath the fracture surface will be simultaneously captured.

To characterize the GB fracture resistance, a penny-shaped crack was initially introduced at the GB. The LEFM solution-based displacement field as shown below is then imposed on the CAC simulation cell to deform it.

https://doi.org/10.1021/acsami.4c17074
ACS Appl. Mater. Interfaces 2025, 17, 2541−2555

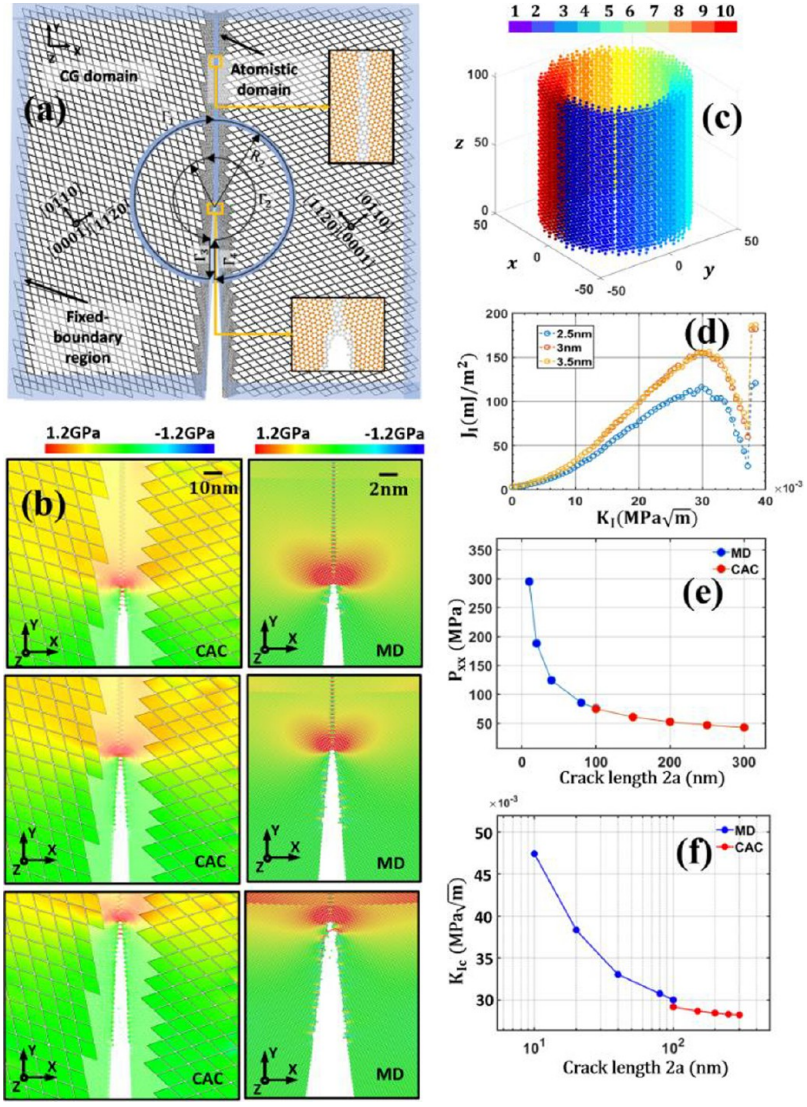

Figure 12. Characterizing the GB crack resistance through CAC simulations: (a) calculating J-integral (noted as J_I) around a GB crack tip in a CAC simulation cell containing a GB crack under Mode-I displacement-controlled loading (noted as K_I). A circular-shaped integration path (light blue) with an inner radius of r and an outer radius of R is chosen to calculate the J-integral ahead of the crack tip; (b) strain sequences of the snapshots resulting from CAC simulations showing the GB crack growth process and its comparison with that from full MD simulations; (c) 3D sketch showing the J-integration path; (d) convergence of J-integral when the inner radius of the J-integration path is increased from 2.5 to 3.0 nm and above; (e) reduction of the peak stress (noted as P_{xx}) upon the increase of the initial crack length (noted as a); and(f) K_{IC}–a relations predicted by MD (blue) and CAC (red) simulations, respectively.

$$u_x = \frac{K_I}{G}\sqrt{\frac{r}{2\pi}}\cos\left(\frac{\theta}{2}\right)\left[1 - 2\nu + \sin^2\left(\frac{\theta}{2}\right)\right] \quad (3)$$

$$u_y = \frac{K_I}{G}\sqrt{\frac{r}{2\pi}}\sin\left(\frac{\theta}{2}\right)\left[1 - 2\nu + \cos^2\left(\frac{\theta}{2}\right)\right] \quad (4)$$

where r and θ are the cylindrical coordinates with the position of the crack tip, and K_I is the mode-I stress intensity factor. G is the shear modulus, and ν is the Poisson's ratio. When the sample is deformed by such a displacement field, first of all, as a demonstration of the CAC's capability in modeling the crack growth in GB under K_I-controlled displacement loading, in Figure 12b, the CAC simulation-predicted GB crack growth process is compared with that from a full MD simulation for a = 50 nm. Clearly, during the process of the GB crack growth, CAC simulations capture the long-range stress ahead of the crack tip together with atomic-level GB structure evolution reasonably well.

To measure the GB fracture resistance, the driving force for GB crack growth will be computed by estimating the J-integral that has been commonly used in LEFM. In detail, the atomistic-informed J-integral[61] along a circular-shaped integration path (inner radius: r; outer radius: R) as shown in Figure 12a is calculated below.

$$\begin{aligned} J &= \int_{\partial\Omega} S\Delta \mathrm{d}A \\ &= \int_{\partial\Omega} (WI - H^T P)\mathrm{d}A \\ &= \sum_{1}^{n_{\text{bins}}} \frac{W}{V_{\text{bin}}} I - \sum_{1}^{n_{\text{bins}}} H^T \frac{P}{V_{\text{bin}}} \end{aligned} \quad (5)$$

https://doi.org/10.1021/acsami.4c17074
ACS Appl. Mater. Interfaces 2025, 17, 2541−2555

where W is the atomistic potential energy, P is the local stress tensor and is calculated using the Virial formula, and F is the deformation gradient. It should be noted that, in CAC, all these quantities can be computed on atoms and FE nodes in the atomic and FE regions, respectively. Numerically, the J-integral path (see a 3D view of it in Figure 12c) ahead of the crack tip in CAC models is discretized into a finite number of bins. The volume of each bin is listed as V_{bin}. Each bin contains a finite number of atoms if it is located within the atomic domain and a number of FE nodes if it is located within the FE domain. Within each bin, W, P, and F acting on atoms and FE nodes are calculated, summed, and then divided by the bin volume, V_{bin}. In this way, the J-integral (the first equality in eq 5) along the chosen integration path can be converted into a summation of the bin values (the second equality in eq 5), where n_{bins} is the total number of bins along the integration path. Such a J-integral retains: (a) the consistent definition of energy, stress, as well as deformation gradient in atomistic and continuum; (b) a path independence of the contour integrals; and (c) an excellent correlation of the CAC simulation data with the theory of fracture mechanics.

As evidence of the path independence of the J-integral, Figure 12d presents the calculated J-integral, noted as J_I, along three different paths (r = 2.5 3.0 nm, and 3.5 nm, respectively), as well as its dependence on the level of the applied loading, K_I. Three main observations in Figure 12d are (a) J_I converges at r = 2.5 nm and above; (b) J_I increases upon the increase of K_I. The J_I−K_I relation obeys the LEFM-based relation very well when K_I is below 15×10^{-3} MPa $\sqrt{m}$; and (c) a sudden drop of J_I, occurs when K_I arrives at a critical value (noted as K_{IC}). For instance, in Figure 12d, for a = 50 nm, $K_{IC} = 30 \times 10^{-3}$ MPa $\sqrt{m}$. This then provides us with opportunities to characterize the initial crack length dependence of the ice GB fracture resistance, i.e., the relationship between K_{IC} and a. It is achieved through three steps: (i) define the J-integration path at the GB crack tip; (ii) record J-integral on the fly of simulations upon the increase of the applied loading in terms of K_I; (iii) perform a series of such simulations with the initial crack length ranging from nanometers to hundreds of nanometers; and (iv) plot the peak stress (noted as P_{xx}) and also K_{IC} at which cracks start to grow as a function of a. The results are presented in Figure 12e and f, respectively. Obviously, both MD and CAC simulations show that K_{IC} decreases upon the increase of a. However, the K_{IC}−a relation does not converge in MD (blue in Figure 12f) due to its limited simulation cell size but converges at a = 300 nm in CAC (red in Figure 12f) due to its capability of scaling up in length.

Instead of focusing on ⟨0001⟩ GB only, as a future attempt, the K_{IC}−a relationship for a variety of GBs can be then extracted from such simulations and then informed into CZFEM[14] to simulate the GB fracture-induced failure of polycrystalline ice at the macroscopic level. In these FE models, the microcracks are initially introduced onto the GBs according to the experimentally characterized distributions in terms of crack lengths and locations. Thereafter, their growth, i.e., the change of crack length, will be dictated by the local stress intensity according to the CAC simulation-based K_{IC}−a relation. In this way, a predictive multiscale computational framework will be established for assessing the overall mechanical behavior of polycrystalline ice at the laboratory scale without smearing out the underlying atomic GB structure diversities.

4. CONCLUSIONS

To conclude, using a well-established three-body mW force field that does not have to explicitly consider the motion of oxygen and hydrogen atoms in water molecules, here, we report the results from a series of CG atomistic computational characterization of ice GB energy, structure, cohesive strength, and their correlation with each other. As a preliminary attempt of scaling up in lengths, a set of CAC simulations are also performed to measure the fracture resistance of the ice GBs containing a crack with lengths ranging from several nanometers to submicrons. Our several main findings are summarized below:

1. The ice GB energy, E_{GB}, exhibits a strong dependence on the misorientation angles, θ. Taking the ⟨0001⟩ GB as an example, it varies from 38 to 60 mJ/m^2 when θ changes from 0 to 60°. Two valleys are observed in the E_{GB}−θ landscape when θ = 21.79° and θ = 32.20°. It suggests that these two ⟨0001⟩ GBs might be the most common GBs in real polycrystalline ice resulting from water freezing;
2. All ⟨0001⟩ STGBs can be considered as a collection of dislocations. The classical Read-Shockley model derived from the theory of elasticity for dislocations can only fit well into the simulation-predicted E_{GB}−θ landscape reasonably well for LAGBs or HAGBs, which contain a relatively lower density of dislocations than that for the GBs with intermediate misorientation angles. The fitting of the atomistic simulation data into the Read-Shockley model will lead to a generalized E_{GB}−θ relation to cover the full spectrum of the θ dependence of the E_{GB};
3. The smallest repeatable structure units (SUs) in ⟨0001⟩ STGBs and their dependence on the misorientation angles are characterized. A critical bond length within the SU, rather than the commonly used E_{GB} or θ, is identified as an indicator that can be used to characterize the GB cohesive strengths. It suggests that the GB structures in realistic noncrystalline ice samples might be well fingerprinted by using the critical bond lengths or the residual strain in such SUs as descriptors;
4. The measurement of the fracture resistance of a GB containing an initial crack is beyond the reach of nanoscale MD simulation because it cannot accommodate the long-range stress carried by a crack in a limited simulation cell. The CAC model furnished with a J-integral calculation scheme can not only scale up in length but also retain the atomistic structure complexity on the GB. It has the potential to characterize the fracture resistance of the GB containing a crack with its length ranging from nanometers to microns.

The above findings provide us with a knowledge database for developing a framework on how to use fine-scale simulations, such as MD and CAC, to characterize the GB energy, structure, cohesive strength, fracture resistance, and their dependence on the misorientation angles in ice. Such information may be then used to calibrate the cohesive laws, such as the one developed by Park, Paulino, and Roesler,[15] or the constitutive rules required by Peridynamics[62,63] for simulating the fracture of polycrystalline ice at the macroscopic level. A translation of the results obtained here into CZFEM or Peridynamics models for polycrystalline ice will go beyond full MD simulations of polycrystalline ice[64] in three aspects: (i) the GBs surveyed here are realistic. By contrast, in a previous

https://doi.org/10.1021/acsami.4c17074
ACS Appl. Mater. Interfaces 2025, 17, 2541−2555

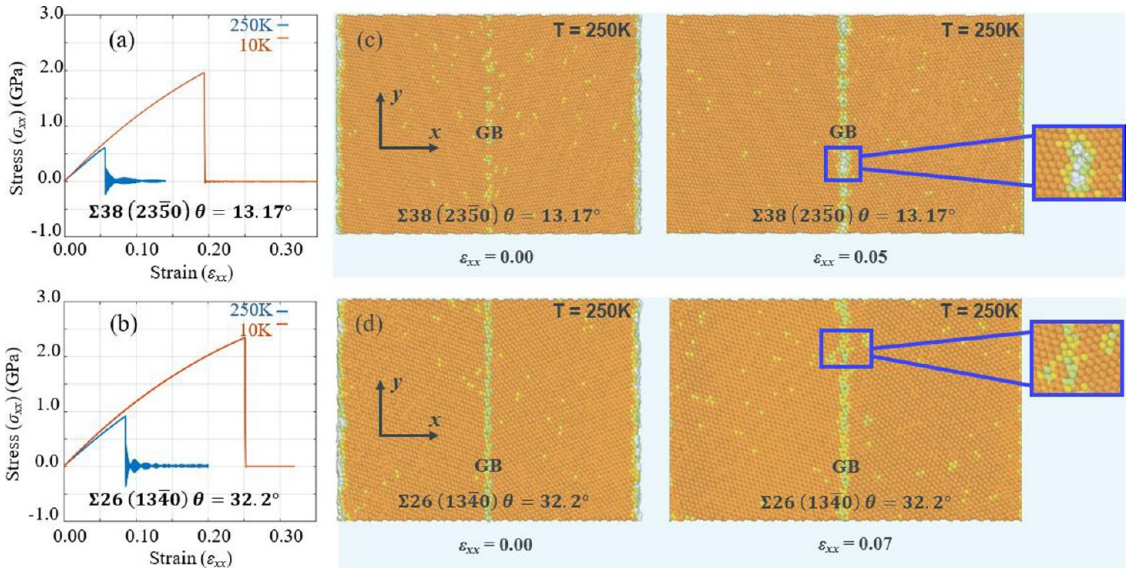

Figure 13. Results from mW-based MD simulations of tensile tests on two different GBs at T = 250 K and T = 10 K: (a, b) stress−strain curves; (c, d) snapshots showing the GB deformation and fracture process. Here, the atoms are color-coded according to their crystallographic orientation. Orange color shows the perfect atomic configuration in ice while the other color shows the deviation away from the perfect atomic configuration.

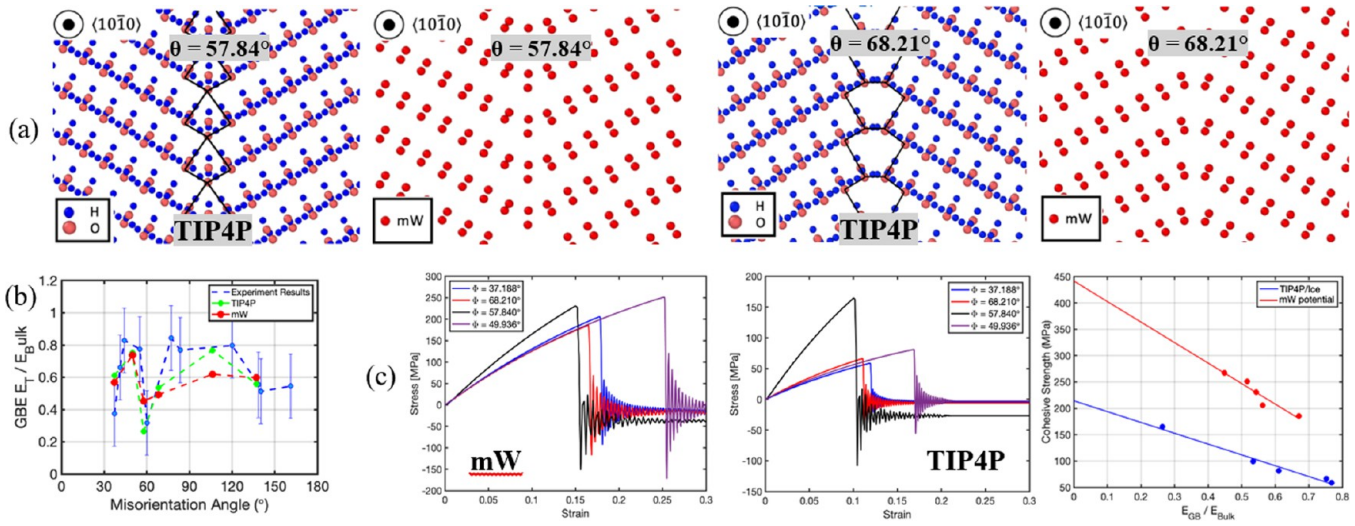

Figure 14. Results from mW-based MD simulations of tensile tests on two different GBs at T = 250 K and T = 10 K: (a, b) stress−strain curves, (c, d) snapshots showing the GB deformation and fracture process. Here, the atoms are color-coded according to their crystallographic orientation. Orange color shows the perfect atomic configuration in ice, while the other color shows the deviation away from the perfect atomic configuration.

study,[64] the authors simply bind two single crystals together in three random misorientations to form the GBs, which may not exist in polycrystalline ice resulting from water freezing; (ii) the misorientation angles of the GBs under consideration here were identified in polycrystalline ice resulting from our MD simulation of water freezing; (iii) as a consequence, informing such GB properties into CZFEM or Peridynamics models for polycrystalline ice will not only scale the grain size up to an experimentally comparable length scale (micro- and millimeters), but also retain the atomistic nature of the realistic GBs in polycrystalline ice implicitly. By contrast, in a previous study,[64] the grain size was only tens of nanometers and the GBs were constructed from Voronoi tessellation. We argue that our preliminary attempt here on integrating MD, CAC, and CAC-informed CZFEM into one framework will provide us with a unique opportunity to perform a quantitative analysis of full-spectrum grain size effects in Hall-Petch behavior of polycrystalline ice containing micrometer- and millimeter-sized grains separated by atomically structured GBs.

Despite its great potential, the above results, however, need to be still taken with caution because

(a) We performed MD simulations at 10 K here. We are fully aware that ice often exists at temperatures much higher than 10 K, and the GB structure/property in it exhibits a strong dependence on temperature or many other environmental conditions. For instance, our preliminary results from the mW-based MD simulations show that the cohesive strengths of the GBs in ice at a temperature of 250 K can be significantly lower than that at 10 K (Figure 13a,b). Due to the finite temperature-induced perturbation, the crack initiation at the GB at 250 K is more localized (see Figure 13c, d) than that at 10 K. GBs often fracture as a whole in a cleavage manner at 10 K. A systematic characterization of the temperature

https://doi.org/10.1021/acsami.4c17074
ACS Appl. Mater. Interfaces 2025, 17, 2541−2555

dependence of GB structure/property will be reported in a separate publication;

(b) By taking the ⟨0001⟩ GB as one example, we obviously have not completed the survey of the whole database for the GBs in polycrystalline ice yet. We recently performed a series of simulations of ice nucleation and growth resulting from water freezing. The detailed grain structure and GB misorientation distribution analysis show that the GB structures in ice exhibit a strong dependence on cooling conditions, chemical impurities, as well as the microstructure of the substrate surface on which the ice forms. A comprehensive characterization of the energy, structure, cohesive strengths, and fracture resistance of those GBs will be needed if a prediction of ice fracture from the bottom up is desired;

(c) All the results in this work are extracted from the simulation of a bicrystalline sample containing an isolate GB. In this setup, the microstructure environment complexity has not been considered. A consideration of the effect of the surrounding microstructure on the GB energy/structure/properties necessitates a tool that can accommodate not only the micron-/millimeter-sized grains but also the atomistic structured GBs within one model. This is nontrivial but can be feasible through CAC simulations, as shown in our previous work[65];

(d) Compared with the commonly used interatomic potential, such as TIP4P,[66] the deployment of the mW force field for water does lead to a significant gain in computational efficiencies. However, the magnitudes of the GB cohesive strengths and fracture resistance resulting from mW force field-based calculations might have been overestimated due to its implicit consideration of the hydrogen bonding between water molecules. To benchmark the accuracy of the mW force field when used for modeling the GBs in ice, we performed full MD simulations using the TIP4P potential where the hydrogen and oxygen atoms were explicitly modeled. GB structures (see Figure 14a), energy (see Figure 14b), and cohesive strengths (see Figure 14c) resulting from such simulations are compared with mW-based MD simulation results. To achieve a one-to-one correspondence between mW and TIP4P force fields, the cutoff in these two fields has been adjusted to the same value. It is shown that (i) mW force field-based MD produced the same GB structure as that from TIP4P-based MD simulations (Figure 14a) but required significantly less computational cost; (ii) the GB energies calculated from MD simulations using mW are comparable to that using TIP4P, both of which exhibit a similar GB disorientation angle dependence as that in experiments (Figure 14b); (iii) although the GB cohesive strengths from both TIP4P- and mW-based MD simulations exhibit a linear dependence on the GB energy, a deployment of mW force field, however, may have overestimated the GB cohesive strengths (Figure 14c). To address this challenge, one approach that we have recently developed is to combine an efficient force field for the material domain (e.g., the mW force field for the grain interior in polycrystalline ice) with the high-fidelity force fields, such as machine learning-based force field,[67] for the material domain nearby the GB.[68] In this way, a trade-off between efficiency and accuracy can be well achieved. We have started expanding our current work in accordance with the above directions and will report the relevant results in future publications.

AUTHOR INFORMATION

Corresponding Authors

Hang Li − *Department of Aerospace Engineering, Iowa State University, Ames, Iowa 50014, United States*; Email: lihang@iastate.edu

Liming Xiong − *Department of Aerospace Engineering, Iowa State University, Ames, Iowa 50014, United States; Department of Mechanical and Aerospace Engineering, North Carolina State University, Raleigh, North Carolina 27695-7001, United States*; orcid.org/0000-0002-9197-6580; Email: lxiong3@ncsu.edu

Authors

Thanh C. Phan − *Department of Aerospace Engineering, Iowa State University, Ames, Iowa 50014, United States; Department of Mechanical and Aerospace Engineering, North Carolina State University, Raleigh, North Carolina 27695-7001, United States*

Ling Zhang − *Silicon Technology Engineering Department, Agoura Hills, California 91301, United States*

Shuozhi Xu − *School of Aerospace and Mechanical Engineering, University of Oklahoma, Norman, Oklahoma 73019, United States*

Ashraf Bastawros − *Department of Aerospace Engineering, Iowa State University, Ames, Iowa 50014, United States*

Hui Hu − *Department of Aerospace Engineering, Iowa State University, Ames, Iowa 50014, United States*

Complete contact information is available at: https://pubs.acs.org/10.1021/acsami.4c17074

Notes

The authors declare no competing financial interest.

ACKNOWLEDGMENTS

H.L., T.P., and L.X. acknowledge the support of the U.S. National Science Foundation (CMMI-2322675 and CMMI-1824840) and the Extreme Science and Engineering Discovery Environment (XSEDE-TG-MSS170003, now MSS170003 at ACCESS). A.B. acknowledges the support of NASA (NNX16AN21A) and the Extreme Science and Engineering Discovery Environment (XSEDE-TG-MSS190008, now MSS190008 at ACCESS). H.H. acknowledges the support of the U.S. National Science Foundation (CMMI-1824840) and the Extreme Science and Engineering Discovery Environment (XSEDE-TG-MSS190013, now MSS190013 at ACCESS). ACCESS is an advanced computing and data resource program supported by the U.S. National Science Foundation under the Office of Advanced Cyberinfrastructure awards 2138259, 2138286, 2138307, 2137603, and 2138296. Discussion with Dr. Yipeng Peng at Iowa State University (now a postdoc at University of Wyoming) is greatly appreciated.

REFERENCES

(1) Andrews, R. Measurement of the fracture toughness of glacier ice. *Journal of Glaciology* **1985**, *31*, 171−176.

(2) Reeh, N.; Thomsen, H. H.; Higgins, A. K.; Weidick, A. Sea ice and the stability of north and northeast Greenland floating glaciers. *Annals of Glaciology* **2001**, *33*, 474−480.

(3) Murton, J. B.; Peterson, R.; Ozouf, J.-C. Bedrock fracture by ice segregation in cold regions. *Science* **2006**, *314*, 1127−1129.

(4) Bjerrum, N. Structure and properties of ice. *Science* **1952**, *115*, 385−390.
(5) Wang, Y.; Liu, X.; Murray, D.; Teng, F.; Jiang, W.; Bachhav, M.; Hawkins, L.; Perez, E.; Sun, C.; Bai, X.; Lian, J.; Judge, C.; Jackson, J.; Carter, R.; He, L. Measurement of grain boundary strength of Inconel X-750 superalloy using in-situ micro-tensile testing techniques in FIB/SEM system. *Materials Science and Engineering: A* **2022**, *849*, No. 143475.
(6) Ketcham, W.; Hobbs, P. An experimental determination of the surface energies of ice. *Philos. Mag.* **1969**, *19*, 1161−1173.
(7) Suzuki, S.; Kuroiwa, D. Grain-boundary energy and grain-boundary groove angles in ice. *Journal of Glaciology* **1972**, *11*, 265−277.
(8) Gonzalez Kriegel, B.; Di Prinzio, C.; Nasello, O. Exact coincidence site lattice in ice Ih. *J. Phys. Chem. B* **1997**, *101*, 6243−6246.
(9) Herring, C.; Kingston, W. *The physics of powder metallurgy*; McGraw Hill: New York, 1951.
(10) Di Prinzio, C. L.; Druetta, E.; Nasello, O. B. Effect of Temperature and Potassium Chloride Impurity on the Relative < $10\bar{1}0$> Tilt Grain Boundary and Surface Free Energies in Ice. *J. Phys. Chem. B* **2014**, *118*, 13365−13370.
(11) Needleman, A. An analysis of tensile decohesion along an interface. *Journal of the Mechanics and Physics of Solids* **1990**, *38*, 289−324.
(12) Barenblatt, G. The mathematical thoery of equilibrium cracks in brittle fracture. *Advances in Applied Mechanics* **1962**, *7*, 55−129.
(13) Schulson, E. Brittle failure of ice. *Engineering Fracture Mechanics* **2001**, *68*, 1839−1887.
(14) Gribanov, I.; Taylor, R.; Sarracino, R. Cohesive zone micromechanical model for compressive and tensile failure of polycrystalline ice. *Engineering Fracture Mechanics* **2018**, *196*, 142−156.
(15) Park, K.; Paulino, G.; Roesler, J. A unified potential-based cohesive model of mixed-mode fracture. *Journal of the Mechanics and Physics of Solids* **2009**, *57*, 891−908.
(16) Falenty, A.; Hansen, T.; Kuhs, W. Formation and properties of ice XVI obtained by emptying a type sII clathrate hydrate. *Nature* **2014**, *516*, 231−233.
(17) Lobban, C.; Finney, J.; Kuhs, W. The structure of a new phase ice. *Nature* **1998**, *391*, 268−270.
(18) Bernal, J.; Fowler, R. A theory of water and ionic solution, with particular reference to hydrogen and hydroxyl ions. *J. Chem. Phys.* **1933**, *1*, 515−548.
(19) Moore, E.; Molinero, V. Structural transformation in supercooled water controls the crystallization rate of ice. *Nature* **2011**, *479*, 506−508.
(20) Lupi, L.; Hudait, A.; Molinero, A. Heterogeneous nucleation of ice on carbon surface. *J. Am. Chem. Soc.* **2014**, *136*, 3156−3164.
(21) Hudait, A.; Allen, M.; Molinero, V. Sink or swim: ions and organics at the ice-air interface. *J. Am. Chem. Soc.* **2017**, *139*, 10095−10103.
(22) Moreira, P.; Veiga, R.; Koning, M. Elastic constants of Ice Ih as described by semi-empirical water models. *J. Chem. Phys.* **2019**, *150*, No. 044503.
(23) Plimpton, S. Fast parallel algorithms for short-range molecular dynamics. *J. Comput. Phys.* **1995**, *117*, 1−19.
(24) Tschopp, M. A.; Tucker, G.; McDowell, D. Structure and free volume of < 110> symmetric tilt grain boundaries with the E structural unit. *Acta Mater.* **2007**, *55*, 3959−3969.
(25) Tschopp, M. A.; Solanki, K. N.; Gao, F.; Sun, X.; Khaleel, M. A.; Horstemeyer, M. F. Probing grain boundary sink strength at the nanoscale: Energetics and length scales of vacancy and interstitial absorption by grain boundaries in α-Fe. *Phys. Rev. B* **2012**, *85*, No. 064108.
(26) Ribeiro, I. d. A.; Koning, M. d. Grain-Boundary Sliding in Ice Ih: Tribology and Rheology at the Nanoscale. *J. Phys. Chem. C* **2021**, *125*, 627−634.
(27) Petrenko, V. F.; Whitworth, R. W. *Physics of ice*; OUP Oxford, 1999.
(28) Suzuki, S. Grain coarsening of microcrystals of ice (III). *Low Temp. Sci. Ser. A* **1970**, *28*, 47−61.
(29) Read, W. T.; Shockley, W. Dislocation models of crystal grain boundaries. *Phys. Rev.* **1950**, *78*, 275.
(30) Humphreys, F. J.; Hatherly, M. *Recrystallization and related annealing phenomena*; Elsevier, 2012.
(31) Bulatov, V. V.; Reed, B. W.; Kumar, M. Grain boundary energy function for fcc metals. *Acta Mater.* **2014**, *65*, 161−175.
(32) Stukowski, A. Visualization and analysis of atomistic simulation data with OVITO−the Open Visualization Tool. *Modell. Simul. Mater. Sci. Eng.* **2010**, *18*, No. 015012.
(33) Maras, E.; Trushin, O.; Stukowski, A.; Ala-Nissila, T.; Jonsson, H. Global transition path search for dislocation formation in Ge on Si (001). *Comput. Phys. Commun.* **2016**, *205*, 13−21.
(34) Sutton, A. P.; Vitek, V. On the structure of tilt grain boundaries in cubic metals I. Symmetrical tilt boundaries. *Philos. Trans. R. Soc. Lond. Ser. A, Math. Phys. Sci.* **1983**, *309*, 1−36.
(35) Inoue, K.; Roh, J.-Y.; Kawahara, K.; Saito, M.; Kotani, M.; Ikuhara, Y. Arrangement of polyhedral units for [0001]-symmetrical tilt grain boundaries in zinc oxide. *Acta Mater.* **2021**, *212*, No. 116864.
(36) Chen, J.; Ruterana, P.; Nouet, G. Structural units and low-energy configurations of [0001] tilt grain boundaries in GaN. *Phys. Rev. B* **2003**, *67*, No. 205210.
(37) Hondoh, T.; Higashi, A. X-Ray diffraction topographic observations of the large-angle grain boundary in ice under deformation. *Journal of Glaciology* **1978**, *21*, 629−638.
(38) Hondoh, T.; Higashi, A. Anisotopy of migration and faceting of large-angle grain boundaries in ice bicrystals. *Philosophical Magazine A* **1979**, *39*, 137−149.
(39) Tsai, D. The virial theorem and stress calculation in molecular dynamics. *J. Chem. Phys.* **1979**, *70*, 1375−1382.
(40) Gammon, P.; Kiefte, H.; Clouter, M. Elastic constants of ice samples by Brillouin spectroscopy. *J. Phys. Chem.* **1983**, *87*, 4025−4029.
(41) Santos-Flórez, P. A.; Ruestes, C. J.; de Koning, M. Uniaxial-deformation behavior of ice I_h as described by the TIP4P/Ice and mW water models. *J. Chem. Phys.* **2018**, *149*, 164711.
(42) Tucker, G. J.; McDowell, D. L. Non-equilibrium grain boundary structure and inelastic deformation using atomistic simulations. *International Journal of Plasticity* **2011**, *27*, 841−857.
(43) Anderson, T. L. *Fracture mechanics: fundamentals and applications*; CRC Press, Taylor and Francis Group, 4th ed., 2017.
(44) Xiong, L.; Chen, Y. Multiscale modeling and simulation of single-crystale MgO through an atomistic field theory. *International Journal of Solids and Structures* **2009**, *46*, 1448−1455.
(45) Xiong, L.; Tucker, G.; McDowell, D.; Chen, Y. Coarse-grained atomistic simulation of dislocations. *Journal of the Mechanics and Physics of Solids* **2011**, *59*, 160−177.
(46) Xiong, L.; Deng, Q.; Tucker, G.; McDowell, D.; Chen, Y. A concurrent scheme for passing dislocations from atomistic to continuum domains. *Acta Mater.* **2012**, *60*, 899−913.
(47) Chen, H.; Xu, S.; Li, W.; Ji, R.; Phan, T.; Xiong, L. A spatial decomposition parallel algorithm for a concurrent atomistic-continuum simulator and its preliminary applications. *Comput. Mater. Sci.* **2018**, *144*, 1−10.
(48) Xu, S.; Xiong, L.; Deng, Q.; McDowell, D. Mesh refinement for the concurrent atomistic-continuum method. *International Journal of Solids and Structures* **2016**, *90*, 144−152.
(49) Su, Y.; Phan, T.; Xiong, L.; Kacher, J. Multiscale computational and experimental analysis of slip-GB reactions: in situ high-resolution electron backscattereed diffraction and concurrent atomistic-continuum simulations. *Scripta Materialia* **2023**, *232*, No. 115500.
(50) Kirkwood, J. The statistical mechanical theory of transport processes I. General Theory. *J. Chem. Phys.* **1946**, *14*, 180−201.
(51) Kirkwood, J. The statistical mechanical theory of transport processes II. Transport in Gases. *J. Chem. Phys.* **1947**, *15*, 72−76.

https://doi.org/10.1021/acsami.4c17074
ACS Appl. Mater. Interfaces 2025, 17, 2541−2555

(52) Kirkwood, J.; Irving, J. The statistical mechanical theory of transport processes. IV. The equations of hydrodynamics. *J. Chem. Phys.* **1950**, *18*, 817−829.
(53) Kirkwood, J.; Bearman, R. Statistical mechanics of transport processes. XI. Equations of transport in multicomponent systems. *J. Chem. Phys.* **1958**, *28*, 136−145.
(54) Chen, Y. Local stress and heat flux in atomistic systems involving three-body forces. *J. Chem. Phys.* **2006**, *124*, No. 054113.
(55) Chen, Y. Reformulation of microscopic balance equations for multiscale materials modeling. *J. Chem. Phys.* **2009**, *130*, 134706.
(56) Chen, Y.; Diaz, A. Physical foundation and consistent formulation of atomic-level fluxes in transport processes. *Physicla Review E* **2018**, *98*, No. 052113.
(57) Yang, S.; Chen, Y. Concurrent atomistic and continuum simulation of bi-crystal strontium titanate with tilt grain boundary. *Proceedings of the Royal Society A: Mathematical, Physical and Engineering Sciences* **2015**, *471*, 20140758.
(58) Xu, S.; Che, R.; Xiong, L.; Chen, Y.; McDowell, D. A quasistatic implementation of the concurrent atomistic-continuum method for fcc crystals. *International Journal of Plasticity* **2015**, *72*, 91−126.
(59) Chen, X.; Diaz, A.; Xiong, L.; McDowell, D.; Chen, Y. Passing waves from atomistic to continuum. *J. Comput. Phys.* **2018**, *354*, 393−402.
(60) Davis, A.; Lloyd, J.; Agrawal, V. Moving window techniques to model shock wave propagation using the concurrent atomistic-continuum method. *Computer Methods in Applied Mechanics and Engineering* **2022**, *389*, No. 114360.
(61) Zimmerman, J.; Jones, R. The application of an atomistic J-integral to a ductile crack. *J. Phys.: Condens. Matter* **2013**, *25*, No. 155402.
(62) Ha, Y.; Bobaru, F. Studies of dynamic crack propagation and crack branching with peridynamics. *Int. J. Fract.* **2010**, *162*, 229−244.
(63) Ha, Y.; Bobaru, F. Characteristics of dynamic brittle fracture captured with peridynamics. *Engineering Fracture Mechanics* **2011**, *78*, 1156−1168.
(64) Cao, P.; Wu, J.; Zhang, Z.; Fang, B.; Peng, L.; Li, T.; Vlugt, T. J. H.; Ning, F. Mechanical properties of bi- and poly-crystalline ice. *AIP Adv.* **2018**, *8*, 125108.
(65) Xiong, L.; Chen, Y.; Lee, J. Modeling and simulation of Boron-doped nanocrystalline silicon carbide thin film by a field theory. *J. Nanosci. Nanotechnol.* **2009**, *9*, 1034−1037.
(66) Abascale, J.; Sanz, E.; Fernandez, R.; Vega, C. A potential model for the study of ices and amorphous water: TIP4P/Ice. *J. Chem. Phys.* **2005**, *122*, 234511.
(67) Chan, H.; Cherukara, M.; Narayanan, B.; Loeffler, T.; Benmore, C.; Gray, S.; Sankaranarayanan, S. Machine learning coarse grained models for water. *Nat. Commun.* **2019**, *10*, 379.
(68) Peng, Y. *An atomistic-to-mesocale predictionof the complex reaction between the plastic flow and the interfaces in heterogeneous materials*. Ph.D. Dissertation, 2022.

https://doi.org/10.1021/acsami.4c17074
ACS Appl. Mater. Interfaces 2025, 17, 2541−2555